

# Study of diffuse H II regions potentially forming part of the gas streams around Sgr A\*

J. Armijos-Abendaño<sup>1\*</sup>, E. López<sup>1</sup>, J. Martín-Pintado<sup>2</sup>, A. Báez-Rubio<sup>3</sup>, M. Aravena<sup>4</sup>, M. A. Requena-Torres<sup>5</sup>, S. Martín<sup>6,7</sup>, M. Llerena<sup>1</sup>, F. Aldás<sup>1</sup>, C. Logan<sup>8</sup> and A. Rodríguez-Franco<sup>9</sup>

<sup>1</sup>Observatorio Astronómico de Quito, Escuela Politécnica Nacional, Av. Gran Colombia S/N, Interior del Parque La Alameda, 170136, Quito, Ecuador

<sup>2</sup>Centro de Astrobiología (CSIC, INTA), Ctra a Ajalvir, km 4, 28850, Torrejón de Ardoz, Madrid, Spain

<sup>3</sup>Instituto de Astronomía, Universidad Nacional Autónoma de México, Circuito de la Investigación Científica s/n, Ciudad Universitaria, Del. Coyoacán, 04510, CDMX, Mexico

<sup>4</sup>Núcleo de Astronomía, Facultad de Ingeniería y Ciencias, Universidad Diego Portales, Av. Ejército 441, Santiago, Chile

<sup>5</sup>Department of Astronomy, University of Maryland, College Park, MD 20742, USA

<sup>6</sup>European Southern Observatory, Alonso de Córdova 3107, Vitacura, Santiago, Chile

<sup>7</sup>Joint ALMA Observatory, Alonso de Córdova 3107, Vitacura, Santiago, Chile

<sup>8</sup>H. H. Wills Physics Laboratory, University of Bristol, Tyndall Ave., Bristol, BS8 1TL, United Kingdom

<sup>9</sup>Facultad de Óptica y Optometría, Departamento de Matemática Aplicada (Biomatemática), Universidad Complutense de Madrid, Avenida de Arcos de Jalón, 118, E-28037 Madrid, Spain

Accepted XXX. Received YYY; in original form ZZZ

## ABSTRACT

We present a study of diffuse extended ionised gas toward three clouds located in the Galactic Centre (GC). One line of sight ( $LOS$ ) is toward the 20 km s<sup>−1</sup> cloud ( $LOS-0.11$ ) in the Sgr A region, another  $LOS$  is toward the 50 km s<sup>−1</sup> cloud ( $LOS-0.02$ ), also in Sgr A, while the third is toward the Sgr B2 cloud ( $LOS+0.693$ ). The emission from the ionised gas is detected from H $\alpha$  and H $m\beta$  radio recombination lines (RRLs). H $\alpha$  and H $m\beta$  RRL emission is detected with the same  $n$  and  $m$  as those from the hydrogen RRLs only toward  $LOS+0.693$ . RRLs probe gas with positive and negative velocities toward the two Sgr A sources. The H $m\beta$  to H $\alpha$  ratios reveal that the ionised gas is emitted under local thermodynamic equilibrium conditions in these regions. We find a He to H mass fraction of  $0.29 \pm 0.01$  consistent with the typical GC value, supporting the idea that massive stars have increased the He abundance compared to its primordial value. Physical properties are derived for the studied sources. We propose that the negative velocity component of both Sgr A sources is part of gas streams considered previously to model the GC cloud kinematics. Associated massive stars with what are presumably the closest H II regions to  $LOS-0.11$  (positive velocity gas),  $LOS-0.02$  and  $LOS+0.693$  could be the main sources of UV photons ionising the gas. The negative velocity components of both Sgr A sources might be ionised by the same massive stars, but only if they are in the same gas stream.

**Key words:** Galaxy: centre – ISM: H II regions – ISM: clouds

## 1 INTRODUCTION

The proximity of the Galactic Centre (GC), at a distance of about 7.86 kpc (Boehle et al. 2016), offers a unique opportunity to look at a galactic nucleus in great detail. Several studies have been carried out to establish the physical properties and the kinematics of ionised gas toward the main compact

H II regions located at the centre of the Galaxy (Ho et al. 1985; Mehringer et al. 1993; Zhao et al. 1993; Mills et al. 2011). Sgr A West, located around the supermassive black hole Sgr A\*, is a spiral-shaped region of ionised gas whose emission is thermal in nature (Ekers et al. 1983). Sgr A East is a non-thermal source surrounding Sgr A West in projection (Ekers et al. 1983). There is also a group of four H II regions, known collectively as G-0.02-0.07, made up of the regions denoted as A, B, C, and D (see Fig. 1, upper

\* E-mail: jairo.armijos@epn.edu.ec

panel). G–0.02–0.07 is located at a projected distance of  $\sim 6$  pc from Sgr A\*. These HII regions likely reside within the  $50 \text{ km s}^{-1}$  cloud<sup>1</sup> (Goss et al. 1985; Mills et al. 2011), one of the massive clouds in the Sgr A complex. Sgr A East may be impacting the  $50 \text{ km s}^{-1}$  cloud at its west side (Serabyn et al. 1992). Massive O stars are thought to be ionising the A–D regions (Lau et al. 2014). Using line to continuum ratios, Goss et al. (1985) found electron temperatures in the range of  $\sim 5000$ – $7000$  K for the four compact HII regions.

Another HII region labelled as G (see Fig. 1, middle panel), located at  $\sim 13$  pc in projection from Sgr A\*, is thought to be excited by one O9 or five B0 stars (Ho et al. 1985). The region G appears to be embedded in the  $20 \text{ km s}^{-1}$  cloud (Armstrong et al. 1989), another massive cloud in the Sgr A complex. Sgr A–E is considered a non-thermal source (Lu et al. 2003), which lies close to the region G (see Fig. 1). Armstrong et al. (1989) found an electron temperature of  $\sim 7500$  K for the region G.

Zhao et al. (1993) studied five HII regions (identified as H1 through to H5) located between Sgr A West and the Arched Filaments HII complex containing a group of curved ridges showing velocities from  $15$  to  $-70 \text{ km s}^{-1}$  (Lang et al. 2001). The H1–H5 sources show gas velocities from  $-20$  to  $-60 \text{ km s}^{-1}$ , which seem to be associated with a  $-30 \text{ km s}^{-1}$  cloud (Zhao et al. 1993). However, negative velocities of the ionised gas are not only observed toward the H1–H5 regions and the Arched Filaments HII complex, as previously thought, but also toward many other regions of the Sgr A complex. In fact, a GC large-scale map obtained by Royster & Yusef-Zadeh (2014) shows ionised gas toward the Sgr A complex with negative velocities reaching up to  $\sim -130 \text{ km s}^{-1}$ . A recent position-velocity map of the CII emission (Langer et al. 2017), which is considered as a good tracer of the ionised gas, shows a similar distribution as in the map obtained by Royster & Yusef-Zadeh (2014). Clouds of diffuse ionised gas in Sgr A with velocities from  $\sim -130$  to  $+130 \text{ km s}^{-1}$  are shown on the channel maps of the CII emission obtained by García (2015).

On the other hand, the Sgr B2 complex lies at a projected distance of  $\sim 120$  pc from the GC. This complex contains many dozens of compact and ultracompact HII regions (Gaume et al. 1995; De Pree et al. 2005). Many of these HII regions are associated with the Sgr B2 north (N), main (M) and south (S) hot cores where star formation is taking place (Gordon et al. 1993). The ionised gas in the Sgr B2 complex shows velocities predominantly in the range of  $50$ – $70 \text{ km s}^{-1}$  (Mehring et al. 1993). There is a HII region labelled as L (Mehring et al. 1993) that is located at a projected distance of  $\sim 1.6$  pc from Sgr B2N (see Fig. 1, bottom panel). The region L has an electron temperature of  $\sim 6500$  K (Mehring et al. 1993) and it is believed to be excited by one O5.5 star (Gaume et al. 1995).

The  $20$  and  $50 \text{ km s}^{-1}$  clouds are considered as part of a set of clouds moving on stable  $x_2$  orbits around the GC in a  $100 \times 60$  pc elliptical and twisted ring (Molinari et al. 2011). In this scenario both clouds are located in the front region of the ring while its background gas, which is around both clouds as seen in projection, show velocities from  $\sim 0$

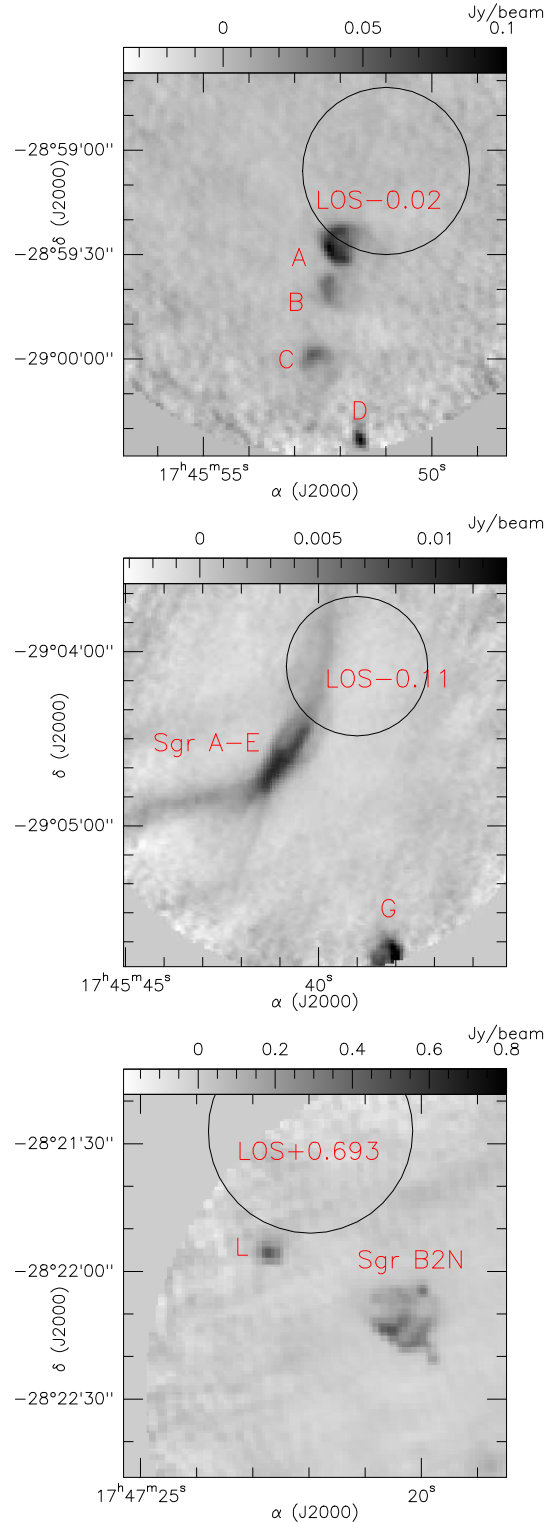


**Figure 1.** VLA radio-continuum maps at 24.5 GHz toward the three LOSs observed by us (see Section 2.1). The three LOSs are shown as black circles with the size of the GBT beam of 48 arcsec at 13.09 GHz. **Upper panel:** The region A partly falls inside LOS–0.02. The regions B, C and D are also seen in the field. **Middle panel:** LOS–0.11 overlaps with part of the non-thermal source Sgr A–E (Lu et al. 2003). The region G appears to be the closest HII region to LOS–0.11 (Ho et al. 1985). **Bottom panel:** LOS+0.693 lies close to the HII region L located northeast of Sgr B2N.

<sup>1</sup> The name is given by its local standard of rest radial velocities.

to  $-60 \text{ km s}^{-1}$  (Molinari et al. 2011). Kruijssen et al. (2015) also modelled the gas kinematics studied by Molinari et al. (2011), reproducing the kinematics of molecular gas using an open gas stream divided into four gas streams orbiting the GC. The back side of the open stream is composed of streams 3 and 4, while streams 1 and 2 are two ends of the open stream located at its front side (Kruijssen et al. 2015). The 20 and  $50 \text{ km s}^{-1}$  clouds are contained in the gas stream 1. A recent study (Langer et al. 2017) revealed that the ionised gas velocities of the Sgr A and Sgr B2 clouds are better explained by the gas streams proposed by Kruijssen et al. (2015) rather than by the elliptical ring proposed by Molinari et al. (2011). Henshaw et al. (2016) found that two spiral arms or gas streams reproduce the molecular gas distribution of several GC clouds. Since no known physical model explains the spiral arms (Henshaw et al. 2016), open streams might be the most likely structure.

In this paper we focus on studying the physical properties and kinematics of the diffuse ionised gas of selected GC regions. Using radio recombination lines (RRLs) observed with the Green Bank Telescope (GBT) of NRAO<sup>2</sup>, we find that RRLs show positive and negative velocities toward two lines of sight (*LOS*) in the Sgr A complex, one toward the  $50 \text{ km s}^{-1}$  cloud (*LOS*−0.02) and another toward the  $20 \text{ km s}^{-1}$  cloud (*LOS*−0.11). We also study the ionised gas along one *LOS* in the Sgr B2 complex (*LOS*+0.693) for comparison purposes. Fig. 1 shows the observed positions of the three *LOS*, where other GC sources are indicated. As indicated in Fig. 1 *LOS*−0.02 covers part of the emission arising from the HII region A. The region G appears to be the closest thermal HII region to *LOS*−0.11 (Ho et al. 1985) since Sgr A–E is considered a non-thermal source in nature (Lu et al. 2003; Yusef-Zadeh et al. 2005). *LOS*+0.693 lies close to the HII region L (see Fig. 1, bottom panel).

This paper is organized as follows. In Section 2 we present the observations and data used in this work. We present the main results in Section 3, focusing on the line identification of RRLs and Gaussian fits in Section 3.1, the local thermodynamic equilibrium of the ionised gas in Section 3.2, helium to hydrogen ratio in Section 3.3, and electron densities and the number of Lyman continuum photons in Section 3.4. We discuss whether the RRL emission detected with the GBT is extended and diffuse in Section 4.1, the kinematics of the ionised gas in Section 4.2, and the sources of gas ionisation in Section 4.3. Finally, the conclusions of this work are presented in Section 5.

## 2 OBSERVATIONS AND DATA REDUCTION

The observations were carried out with the NRAO 100-m Green Bank Telescope (GBT) in July–October 2009. We used the Ku-band receiver connected to the spectrometer that provided four 200 MHz spectral windows in two polarizations. This configuration provides a spectral resolution of 24.4 kHz or  $0.6 \text{ km s}^{-1}$ . Spectra were calibrated using a noise tube and the line intensities, affected by 20 per cent uncertainties, are given in  $T_A^*$  scale. The position-switched

**Table 1.** Observed positions and their references

Source	Position		Reference	
	RA(J2000)	DEC(J2000)	RA(J2000)	DEC(J2000)
<i>LOS</i> −0.02	17 <sup>h</sup> 45 <sup>m</sup> 51.0 <sup>s</sup>	−28°59′06.0″	17 <sup>h</sup> 46 <sup>m</sup> 00.1 <sup>s</sup>	−29°16′47.2″
<i>LOS</i> −0.11	17 <sup>h</sup> 45 <sup>m</sup> 39.0 <sup>s</sup>	−29°04′05.0″	17 <sup>h</sup> 46 <sup>m</sup> 00.1 <sup>s</sup>	−29°16′47.2″
<i>LOS</i> +0.693	17 <sup>h</sup> 47 <sup>m</sup> 22.0 <sup>s</sup>	−28°21′27.0″	17 <sup>h</sup> 46 <sup>m</sup> 23.0 <sup>s</sup>	−28°16′37.3″

mode was used during the observations. As mentioned, the studied *LOS*s are shown in Fig. 1. The angular resolution is 45 arcsec at 14.19 GHz, which corresponds to  $\sim 1.7 \text{ pc}$  at the distance of the GC. We used the reference positions selected and verified by Martín et al. (2008), which were originally based on large scale CS maps (Bally et al. 1987). The three observed *LOS* positions and their reference positions are indicated in Table 1.

Using the GBTIDL package<sup>3</sup>, we inspected all scans of the SDFITS files, and the baseline subtraction and average were applied to the calibrated spectra. Then the data were imported into the MADCUBA package<sup>4</sup> for further processing. The spectra were smoothed to a velocity resolution of  $\sim 5 \text{ km s}^{-1}$  appropriate for the RRL widths,  $\Delta v_r$ , of  $\sim 30 \text{ km s}^{-1}$  observed in the GC (Mehring et al. 1993).

### 2.1 Archival VLA data

To find out whether the emission detected with the GBT is affected by emission arising from compact HII regions (see discussion in Section 4.1), we have used VLA data at 24.5 GHz available in the NRAO archive<sup>5</sup>. The VLA data reduction and imaging were done using the CASA package<sup>6</sup> (version 4.7.0). The observations were carried out in 2012 using the DnC configuration. We have build continuum maps, shown in Fig. 1, and also a H64 $\alpha$  cube for the *LOS*−0.02 region as this information will be required in Section 4.1. The continuum maps and cube were obtained using the `clean` task of CASA. The spatial resolution of the maps and cube is  $2.52 \times 2.47 \text{ arcsec}^2$ . The cube has a rms noise of  $\sim 4 \text{ mJy beam}^{-1}$  per channel, while the continuum maps of both Sgr A regions and the *LOS*+0.693 region have rms noises of  $\sim 2$  and  $\sim 20 \text{ mJy beam}^{-1}$ , respectively.

## 3 RESULTS

### 3.1 Line identification and Gaussian fits

To identify hydrogen (H) and helium (He) RRLs we have used a catalog included in the MADCUBAIIJ package, which contains the frequencies of the RRLs estimated according to the Dirac theory described by Towle et al. (1996). The RRLs detected in *LOS*−0.11, *LOS*−0.02 and *LOS*+0.693 are shown in Fig. 2, 3 and 4–5, respectively. We have detected emission from Hn $\alpha$  lines with  $n=79-75$  and Hm $\beta$

<sup>2</sup> The National Radio Astronomy Observatory is a facility of the National Science Foundation, operated under a cooperative agreement by Associated Universities, Inc.

<sup>3</sup> GBTIDL is an NRAO data reduction package, written in the IDL language for the reduction of GBT data.

<sup>4</sup> This package have been developed at the Centro de Astrobiología. More information about this package in <http://cab.inta-csic.es/madcuba/Portada.html>.

<sup>5</sup> <https://archive.nrao.edu/>

<sup>6</sup> <http://casa.nrao.edu/>

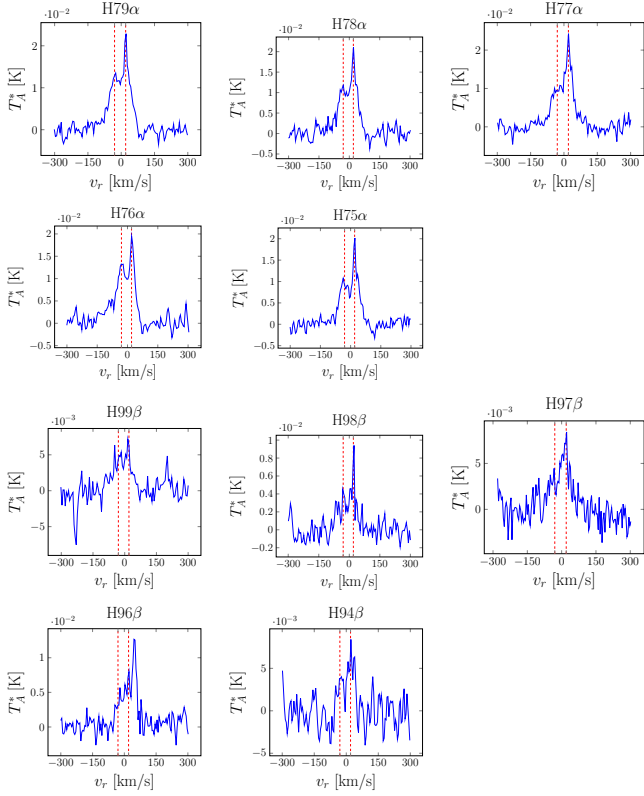


**Figure 2.** Hydrogen RRLs observed toward  $LOS-0.11$ . The dashed red lines show the velocities of 20 and  $-30 \text{ km s}^{-1}$ . The spectra are shown with a spectral resolution of  $\sim 5 \text{ km s}^{-1}$ .

lines with  $m=99-96$ , 94 toward  $LOS-0.11$  and  $LOS-0.02$ . Hydrogen RRLs with the same  $n$  and  $m$  are also detected toward  $LOS+0.693$  but, in this case, we have also detected the  $H95\beta$ , whose frequency is not in the bandwidth of our observations toward either of the two Sgr A sources. All these RRLs are detected with a significance higher than  $3\sigma$ . The strongest RRLs are observed in  $LOS+0.693$ , whereas the weakest lines are detected in  $LOS-0.11$ . We have detected the emission from  $\text{He}n\alpha$  lines, with  $n=79-75$  and  $\text{He}m\beta$  lines with  $m=99-94$ , only toward  $LOS+0.693$  (see Fig. 5). As shown in Fig. 2 and 3 the RRLs in both of the of Sgr A sources reveal two velocity components, while the RRLs in  $LOS+0.693$  show only a single velocity component.

Gaussian fits to the RRLs are used to derive the peak intensity ( $T_A^*$ ), central line velocity ( $v_r$ ), full width at half maximum ( $\Delta v_r$ ), the integrated line intensity ( $\int T_A^* dv_r$ ), and their respective uncertainties. The frequencies of the RRLs and the derived parameters for each source are listed in Tables 2–4. The RRLs found in both sources of Sgr A are fitted with two Gaussian lines. The two velocity components are labelled as  $+20$  and  $-30 \text{ km s}^{-1}$  in  $LOS-0.11$  and as  $+50$  and  $-40 \text{ km s}^{-1}$  in  $LOS-0.02$  in Tables 7, 9 and 10. As mentioned,  $\text{He}n\alpha$  lines are detected only in  $LOS+0.693$ , and the parameters derived using Gaussian fits are given in Table 5, where upper limits for the  $T_A^*$  and  $\int T_A^* dv_r$  of the  $\text{He}94\beta$  line are also listed. For both sources of Sgr A we have estimated  $3\sigma$  upper limits for  $T_A^*$  of the He lines shown in Table 6 because we will study the He to H ratio in Section 3.3. In

**Table 2.** Hydrogen RRL parameters derived for  $LOS-0.11$  using Gaussian fits with two velocity components.

RRL	$\nu$ (GHz)	$T_A^*$ (mK)	$v_r$ ( $\text{km s}^{-1}$ )	$\Delta v_r$ ( $\text{km s}^{-1}$ )	$\int T_A^* dv_r$ ( $\times 10^2 \text{ mK km s}^{-1}$ )
H79 $\alpha$	13.09	$19.4 \pm 1.6$ $12.6 \pm 1.3$	$22.9 \pm 1.3$ $-26.5 \pm 2.5$	$30.2 \pm 2.9$ $49.7 \pm 6.5$	$6.2 \pm 0.8$ $6.7 \pm 1.2$
H78 $\alpha$	13.60	$17.9 \pm 0.9$ $11.0 \pm 0.8$	$21.9 \pm 1.3$ $-32.3 \pm 2.4$	$38.2 \pm 2.8$ $48.6 \pm 5.7$	$7.3 \pm 0.7$ $5.7 \pm 0.8$
H77 $\alpha$	14.12	$22.9 \pm 3.5$ $9.8 \pm 1.1$	$21.8 \pm 0.8$ $-17.2 \pm 9.1$	$27.3 \pm 2.6$ $80 \pm 17$	$6.6 \pm 1.3$ $8.4 \pm 2.2$
H76 $\alpha$	14.69	$19.0 \pm 1.1$ $13.1 \pm 1.0$	$22.9 \pm 1.2$ $-28.7 \pm 1.9$	$29.9 \pm 2.7$ $51.3 \pm 4.8$	$6.1 \pm 0.7$ $7.2 \pm 0.9$
H75 $\alpha$	15.28	$20.0 \pm 1.0$ $10.4 \pm 0.8$	$22.5 \pm 0.9$ $-32.5 \pm 2.0$	$30.0 \pm 2.0$ $51.6 \pm 5.3$	$6.4 \pm 0.6$ $5.7 \pm 0.8$
H99 $\beta$	13.15	$5.9 \pm 1.1$ $4.7 \pm 0.5$	$17.3 \pm 3.5$ $-30.0 \pm 6.0$	$25.8 \pm 7.1$ $50 \pm 13$	$1.6 \pm 0.6$ $2.5 \pm 0.8$
H98 $\beta$	13.56	$9.0 \pm 0.9$ $3.3 \pm 0.6$	$20.2 \pm 1.7$ $-30.0 \pm 5.2$	$25.1 \pm 4.2$ $50 \pm 14$	$2.4 \pm 0.5$ $1.8 \pm 0.6$
H97 $\beta$	13.98	$8.1 \pm 1.0$ $3.0 \pm 0.5$	$17.4 \pm 1.6$ $-30.0 \pm 8.7$	$37.0 \pm 3.8$ $50 \pm 19$	$3.2 \pm 0.6$ $1.6 \pm 0.7$
H96 $\beta$	14.41	$7.6 \pm 0.9$ $3.7 \pm 0.6$	$16.9 \pm 2.4$ $-30.0 \pm 7.3$	$29.0 \pm 8.3$ $50 \pm 16$	$2.3 \pm 0.8$ $1.9 \pm 0.7$
H94 $\beta$	15.34	$5.7 \pm 0.6$ $4.0 \pm 1.0$	$22.4 \pm 2.6$ $-30.0 \pm 3.7$	$35.8 \pm 6.1$ $50.0 \pm 9.2$	$2.1 \pm 0.5$ $2.2 \pm 0.8$

**Table 3.** Hydrogen RRL parameters derived for  $LOS-0.02$  using Gaussian fits with two velocity components.

RRL	$\nu$ (GHz)	$T_A^*$ (mK)	$v_r$ ( $\text{km s}^{-1}$ )	$\Delta v_r$ ( $\text{km s}^{-1}$ )	$\int T_A^* dv_r$ ( $\times 10^2 \text{ mK km s}^{-1}$ )
H79 $\alpha$	13.09	$92.8 \pm 3.5$ $45.6 \pm 2.3$	$46.1 \pm 0.5$ $-39.2 \pm 1.4$	$27.6 \pm 1.1$ $60.6 \pm 3.4$	$27.2 \pm 1.7$ $29.4 \pm 2.3$
H78 $\alpha$	13.60	$83.0 \pm 2.9$ $42.9 \pm 2.0$	$46.6 \pm 0.5$ $-41.0 \pm 1.3$	$29.7 \pm 1.1$ $61.9 \pm 3.1$	$26.3 \pm 1.4$ $28.2 \pm 2.0$
H77 $\alpha$	14.12	$72.8 \pm 1.7$ $28.1 \pm 1.2$	$45.6 \pm 0.4$ $-39.8 \pm 1.3$	$31.8 \pm 0.9$ $61.8 \pm 3.3$	$24.6 \pm 1.0$ $18.5 \pm 1.3$
H76 $\alpha$	14.69	$73.6 \pm 2.1$ $30.8 \pm 1.5$	$46.5 \pm 0.4$ $-41.6 \pm 1.4$	$29.5 \pm 1.0$ $63.3 \pm 3.2$	$23.1 \pm 1.1$ $20.8 \pm 1.5$
H75 $\alpha$	15.28	$57.4 \pm 2.1$ $34.6 \pm 1.6$	$48.1 \pm 0.6$ $-39.8 \pm 1.2$	$32.1 \pm 1.3$ $57.0 \pm 2.9$	$19.6 \pm 1.2$ $21.0 \pm 1.5$
H99 $\beta$	13.15	$23.1 \pm 2.2$ $9.6 \pm 1.5$	$48.1 \pm 1.2$ $-40.0 \pm 4.1$	$24.4 \pm 2.8$ $60.0 \pm 9.6$	$6.0 \pm 0.9$ $6.2 \pm 1.4$
H98 $\beta$	13.56	$24.4 \pm 1.1$ $11.1 \pm 0.8$	$45.6 \pm 0.6$ $-40.3 \pm 1.9$	$31.4 \pm 1.5$ $59.6 \pm 4.4$	$8.2 \pm 0.6$ $7.1 \pm 0.8$
H97 $\beta$	13.98	$20.2 \pm 0.9$ $7.9 \pm 0.7$	$46.0 \pm 0.6$ $-37.9 \pm 2.0$	$28.9 \pm 1.4$ $53.6 \pm 4.7$	$6.2 \pm 0.4$ $4.5 \pm 0.6$
H96 $\beta$	14.41	$20.3 \pm 1.0$ $8.9 \pm 0.9$	$48.3 \pm 0.7$ $-31.0 \pm 2.8$	$30.5 \pm 1.6$ $56.2 \pm 7.1$	$6.6 \pm 0.5$ $5.3 \pm 0.6$
H94 $\beta$	15.34	$14.6 \pm 1.3$ $8.3 \pm 1.0$	$51.4 \pm 1.4$ $-40.2 \pm 2.8$	$35.4 \pm 3.4$ $60.0 \pm 6.6$	$5.5 \pm 0.8$ $5.3 \pm 0.9$

**Table 4.** Hydrogen RRL parameters derived for  $LOS+0.693$  using Gaussian fits.

RRL	$\nu$ (GHz)	$T_A^*$ (mK)	$v_r$ ( $\text{km s}^{-1}$ )	$\Delta v_r$ ( $\text{km s}^{-1}$ )	$\int T_A^* dv_r$ ( $\times 10^3 \text{ mK km s}^{-1}$ )
H79 $\alpha$	13.09	$441.6 \pm 3.2$	$71.4 \pm 0.1$	$31.0 \pm 0.3$	$14.6 \pm 0.2$
H78 $\alpha$	13.60	$401.4 \pm 3.1$	$71.8 \pm 0.1$	$32.0 \pm 0.3$	$13.7 \pm 0.2$
H77 $\alpha$	14.12	$382.0 \pm 4.8$	$71.8 \pm 0.2$	$31.0 \pm 0.4$	$12.6 \pm 0.2$
H76 $\alpha$	14.69	$383.3 \pm 6.5$	$71.7 \pm 0.2$	$30.7 \pm 0.6$	$12.5 \pm 0.3$
H75 $\alpha$	15.28	$350.4 \pm 2.5$	$72.3 \pm 0.1$	$30.0 \pm 0.3$	$11.2 \pm 0.1$
H99 $\beta$	13.15	$93.2 \pm 3.1$	$70.2 \pm 0.5$	$37.0 \pm 1.3$	$3.7 \pm 0.2$
H98 $\beta$	13.56	$91.1 \pm 1.0$	$71.8 \pm 0.3$	$33.0 \pm 0.4$	$3.2 \pm 0.1$
H97 $\beta$	13.98	$88.4 \pm 3.7$	$71.3 \pm 0.4$	$32.2 \pm 1.0$	$3.0 \pm 0.1$
H96 $\beta$	14.41	$84.5 \pm 1.8$	$73.5 \pm 0.4$	$37.4 \pm 0.8$	$3.4 \pm 0.1$
H95 $\beta$	14.87	$91.9 \pm 2.8$	$72.0 \pm 0.4$	$30.5 \pm 1.0$	$3.0 \pm 0.1$
H94 $\beta$	15.34	$78.5 \pm 1.0$	$72.6 \pm 0.2$	$32.0 \pm 0.5$	$2.7 \pm 0.1$



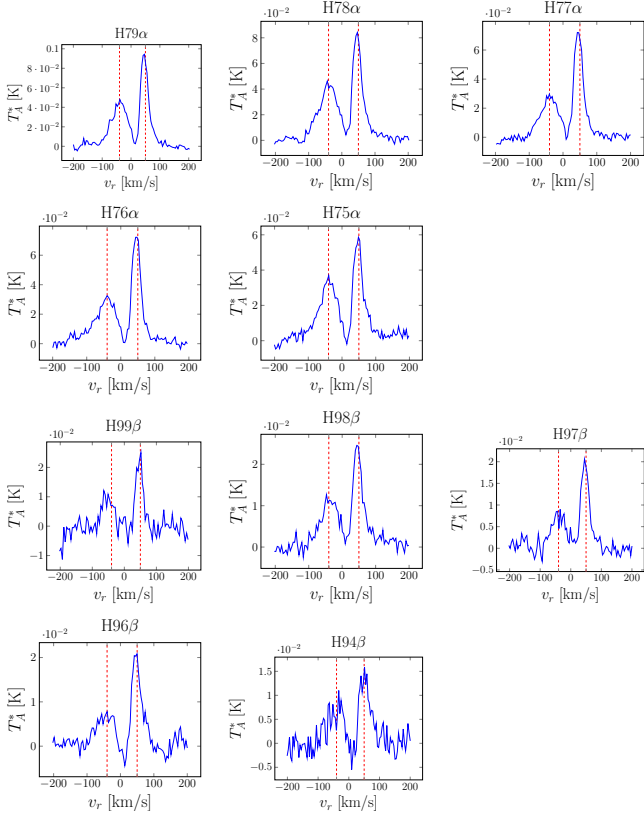


**Figure 3.** Hydrogen RRLs observed toward  $LOS-0.02$ . The dashed red lines show the velocities of 50 and  $-40 \text{ km s}^{-1}$ . The spectra are shown with a spectral resolution of  $\sim 5 \text{ km s}^{-1}$ .

**Table 5.** Helium RRL parameters derived for  $LOS+0.693$  using Gaussian fits.

RRL	$\nu$ (GHz)	$T_A^*$ (mK)	$v_r$ ( $\text{km s}^{-1}$ )	$\Delta v_r$ ( $\text{km s}^{-1}$ )	$\int T_A^* dv_r$ ( $\times 10^2 \text{ mK km s}^{-1}$ )
He79 $\alpha$	13.09	$31.8 \pm 2.0$	$71.5 \pm 0.7$	$26.6 \pm 1.6$	$9.0 \pm 0.8$
He78 $\alpha$	13.60	$35.8 \pm 2.9$	$73.5 \pm 0.9$	$26.0 \pm 2.0$	$9.9 \pm 1.2$
He77 $\alpha$	14.13	$28.2 \pm 3.9$	$73.0 \pm 1.6$	$26.8 \pm 3.7$	$8.0 \pm 1.7$
He76 $\alpha$	14.70	$23.4 \pm 1.8$	$72.8 \pm 0.8$	$25.2 \pm 1.9$	$6.3 \pm 0.7$
He75 $\alpha$	15.29	$24.3 \pm 5.4$	$72.3 \pm 2.3$	$23.3 \pm 5.4$	$6.0 \pm 2.0$
He99 $\beta$	13.15	$7.1 \pm 3.5$	$65.7 \pm 5.6$	$30 \pm 13$	$2.3 \pm 1.6$
He98 $\beta$	13.56	$9.5 \pm 2.1$	$70.8 \pm 1.9$	$22.2 \pm 4.6$	$2.2 \pm 0.7$
He97 $\beta$	13.98	$8.0 \pm 2.7$	$66.6 \pm 4.5$	$27 \pm 11$	$2.3 \pm 1.3$
He96 $\beta$	14.42	$7.7 \pm 1.2$	$70.2 \pm 3.1$	$21.7 \pm 3.1$	$1.8 \pm 0.4$
He95 $\beta$	14.87	$7.8 \pm 1.3$	$71.8 \pm 1.1$	$17.4 \pm 2.5$	$1.4 \pm 0.3$
He94 $\beta$	15.35	$< 6.5^{(a)}$	...	...	$< 1.7^{(b)}$

<sup>(a)</sup>  $3\sigma$  upper limit on the line intensity.

<sup>(b)</sup>  $3\sigma$  upper limit on the velocity-integrated line intensity.

Table 6 there are no upper limits for the He95 $\beta$  line as it was not observed in either of the Sgr A sources.

### 3.2 LTE conditions

In order to check whether local thermodynamic equilibrium (LTE) conditions apply in the three GC sources, we have derived the  $Hm\beta$  to  $Hn\alpha$  integrated line intensity ratios (hereafter  $Hm\beta$  to  $Hn\alpha$  ratios), using  $Hn\alpha$  and  $Hm\beta$  lines that were observed simultaneously to avoid uncertainties related to pointing and flux calibration. We show the value of these ratios in Table 7 for the different velocity components and

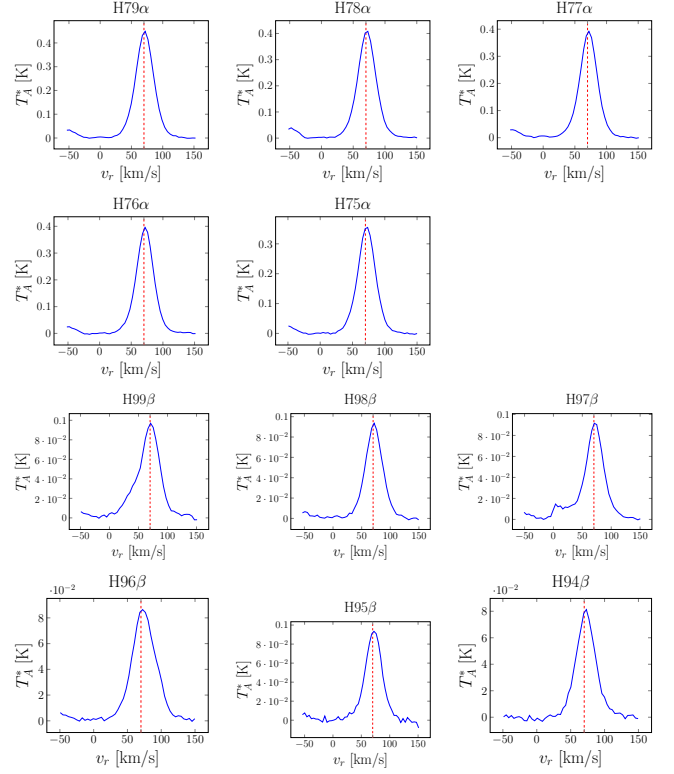


**Figure 4.** Hydrogen RRLs observed toward  $LOS+0.693$ . The dashed red line shows the velocity of  $70 \text{ km s}^{-1}$ . The spectra are shown with a spectral resolution of  $\sim 5 \text{ km s}^{-1}$ .

**Table 6.**  $3\sigma$  upper limits on the He line intensities for  $LOS-0.11$  and  $LOS-0.02$ .

RRL	$\nu$ (GHz)	$LOS-0.11$	$LOS-0.02$
		$T_A^*$ (mK)	$T_A^*$ (mK)
He79 $\alpha$	13.09	$< 5$	$< 11$
He78 $\alpha$	13.60	$< 3$	$< 9$
He77 $\alpha$	14.13	$< 11$	$< 5$
He76 $\alpha$	14.70	$< 3$	$< 6$
He75 $\alpha$	15.29	$< 3$	$< 6$
He99 $\beta$	13.15	$< 3$	$< 8$
He98 $\beta$	13.56	$< 3$	$< 3$
He97 $\beta$	13.98	$< 3$	$< 3$
He96 $\beta$	14.42	$< 3$	$< 3$
He94 $\beta$	15.35	$< 3$	$< 4$

the three GC sources. In this table we also list the  $Hm\beta$  to  $Hn\alpha$  ratios estimated assuming LTE conditions and optically thin radio continuum emission. We also show the  $Hm\beta$  to  $Hn\alpha$  integrated line intensity ratios for  $LOS+0.693$  in Table 8, where the expected LTE values are also listed.

As seen in Table 7, the three GC sources have  $Hm\beta$  to  $Hn\alpha$  ratios that are consistent, within their uncertainties, with those predicted in LTE, but there are values (in bold print) in this table that do not match the expected LTE ratio. In  $LOS-0.02$ , the measured H99 $\beta$  to H79 $\alpha$  and H98 $\beta$  to H78 $\alpha$  (positive velocity component) ratios are inconsistent with the LTE values likely due to uncertainty in the

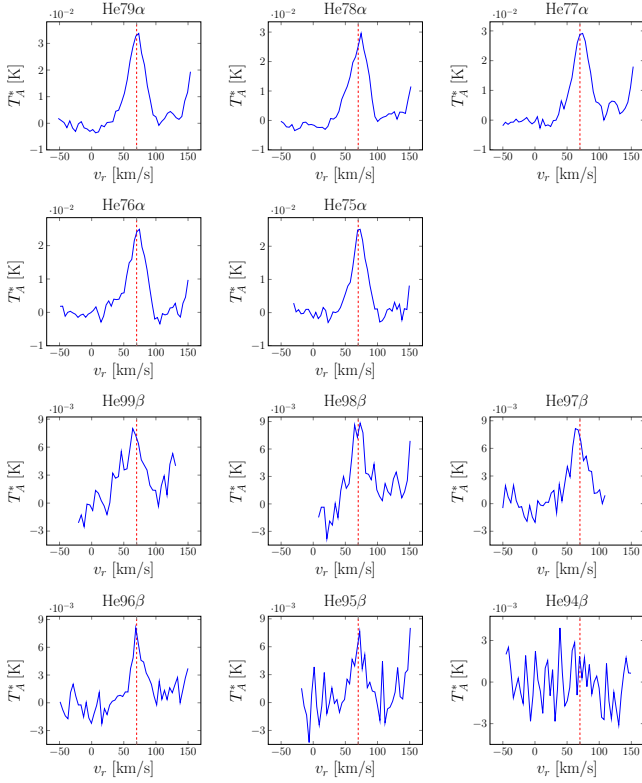


**Figure 5.** Helium RRLs observed toward  $LOS+0.693$ . The dashed red line shows the velocity of  $70 \text{ km s}^{-1}$ . The spectra are shown with a spectral resolution of  $\sim 5 \text{ km s}^{-1}$ .

baseline correction of the H99 $\beta$  and H98 $\beta$  lines. The same reason may explain why the H99 $\beta$ , H98 $\beta$ , and H94 $\beta$  lines, in  $LOS+0.693$ , show intensities lower than those expected in LTE. On the other hand, the measured  $Hm\beta$  to  $Hn\alpha$  ratios (see Table 8) are consistent within their uncertainties with the values expected in LTE. In summary, the  $Hm\beta$  to  $Hn\alpha$  ratios derived for the three GC sources and the  $Hm\beta$  to  $Hn\alpha$  ratios derived for  $LOS+0.693$  show that the ionised gas in the studied sources can be reasonably assumed to be emitted under LTE conditions.

### 3.3 Helium to hydrogen ratio

As mentioned above, helium RRLs have only been detected toward  $LOS+0.693$ . We have derived the He-to-H line intensity ratios (see Table 9) for those RRL transitions where the same principal quantum number has been detected for the two elements. Otherwise, we provide upper limits assuming that the line intensity of the non-detected RRLs is lower than  $3\sigma$ . We note that the  $Hn\alpha$  RRLs are located at  $\approx 122 \text{ km s}^{-1}$  with respect to  $Hn\alpha$  RRLs, as expected by the difference of their rest frequencies (Towle et al. 1996). Thus, the derived ratios are not affected by possible effects of calibration since both spectral lines are observed simultaneously at close frequencies.

We find an average He-to-H intensity ratio of  $7.3 \pm 0.2$  per cent or  $^4\text{He}$  mass fraction  $Y = 0.29 \pm 0.01$  for  $LOS+0.693$ . This ratio is consistent with those found in interferometry studies (Roelfsema et al. 1987; Mehringer et al. 1993)

that trace more compact regions ( $\lesssim 0.7 \text{ pc}$ ) than our diffuse regions ( $\sim 1.7 \text{ pc}$ ). The most stringent upper limits on the He-to-H ratio derived for  $LOS-0.02$  and  $LOS-0.11$  are consistent with the He-to-H number ratio of  $<10$  per cent found in GC HII regions (Roelfsema et al. 1987). The estimation of  $0.29 \pm 0.01$  helium abundance by mass differs by 14 per cent from that of 0.25 as predicted by Big Bang nucleosynthesis (Coc et al. 2012; Tsivilev et al. 2013). This finding suggests, as expected (Wilson & Rood 1994; Gordon & Soroichenko 2009), that high-mass stars in the GC have enriched the ISM with helium-4, in a past intense burst of star formation in this region, thus increasing its abundance compared to the primordial value.

### 3.4 Electron densities and number of Lyman ionising photons

In this section we derive the average electron density  $n_e$  of the ionised gas following the equation as in Mezger & Henderson (1967), where  $n_e$  is given by:

$$\left(\frac{n_e}{\text{cm}^{-3}}\right) = 6.351 \cdot 10^2 u_1 a^{0.5} \left(\frac{T_e}{10^4 \text{ K}}\right)^{0.175} \left(\frac{\nu}{\text{GHz}}\right)^{0.05} \left(\frac{S_c}{\text{Jy}}\right)^{0.5} \left(\frac{D}{\text{kpc}}\right)^{-0.5} \left(\frac{\Theta}{\text{arcmin}}\right)^{-1.5}, \quad (1)$$

where  $T_e$  is the electron temperature,  $\nu$  is the frequency,  $S_c$  is the continuum flux,  $D$  is the distance to the GC (7.86 kpc, Boehle et al. (2016)) and  $\Theta$  is the source size (which is assumed to be equal to the telescope beam size corresponding to  $\approx 1.7 \text{ pc}$  at the GC distance). The parameter  $a$  accounts for the deviation between the exact equation for the optical depth for free-free emission and its approximation (Mezger & Henderson 1967). For our study we have used an average value of  $a$  equal to 0.98. We have assumed that our three GC sources have spherical geometry, and in this case the model conversion factor  $u_1$  is equal to 0.775 (Mezger & Henderson 1967). The  $S_c$  is derived from the H77 $\alpha$  and H96 $\beta$  RRL emission assuming an optically thin regime and the average  $T_e$  found for compact HII regions of the GC, i.e.  $T_e \approx 6300 \text{ K}$  (Goss et al. 1985).  $S_c$  values derived from the H77 $\alpha$  and H96 $\beta$  RRLs are similar, within their uncertainties, to those obtained from the other detected  $Hn\alpha$  and  $Hm\beta$  lines, respectively. For this reason Table 10 lists only the  $S_c$  values derived from the H77 $\alpha$  and H96 $\beta$  lines. For the three GC sources the estimated values of  $n_e$  are given in Table 10.

Using the formula given in Rohlfs & Wilson (1999) (see Eq. 13.2) we have also calculated the number of Lyman ionising photons,  $N_{\text{Lyc}}$ , as follows:

$$N_{\text{Lyc}} = \frac{4}{3} \pi \left(\frac{\Theta}{2}\right)^3 n_e n_p \alpha^{(2)}, \quad (2)$$

where  $n_p$  is the proton density (which is equal to  $n_e$  under LTE conditions, see Section 3.2), and  $\alpha^{(2)}$  is the recombination coefficient (Spitzer 2004). The derived values of  $N_{\text{Lyc}}$  for the three GC sources are shown in Table 10.

**Table 7.**  $Hm\beta/Hn\alpha$  ratios for the three GC  $LOS$ s

Ratio	Model <sup>(a)</sup> (%)	$LOS-0.11$		$LOS-0.02$		$LOS+0.693$	
		$v_r^{(b)}$ (km s <sup>-1</sup> )	$\frac{I_{Hm\beta}}{I_{Hn\alpha}}$ (%)	$v_r^{(b)}$ (km s <sup>-1</sup> )	$\frac{I_{Hm\beta}}{I_{Hn\alpha}}$ (c) (%)	$v_r^{(b)}$ (km s <sup>-1</sup> )	$\frac{I_{Hm\beta}}{I_{Hn\alpha}}$ (c) (%)
H99 $\beta$ /H79 $\alpha$	27.3	+20	25.8 $\pm$ 9.8	+50	<b>22.1<math>\pm</math>3.7</b>	+70	<b>25.2<math>\pm</math>1.3</b>
		-30	37 $\pm$ 13	-40	<b>20.9<math>\pm</math>5.2</b>		
H98 $\beta$ /H78 $\alpha$	27.0	+20	33.0 $\pm$ 7.6	+50	<b>31.1<math>\pm</math>2.7</b>	+70	<b>23.4<math>\pm</math>0.5</b>
		-30	31 $\pm$ 11	-40	25.0 $\pm$ 3.2		
H96 $\beta$ /H77 $\alpha$	27.7	+20	35 $\pm$ 13	+50	26.8 $\pm$ 2.3	+70	26.7 $\pm$ 1.0
		-30	23 $\pm$ 11	-40	28.8 $\pm$ 3.9		
H96 $\beta$ /H76 $\alpha$	26.6	+20	39 $\pm$ 13	+50	28.6 $\pm$ 2.5	+70	26.8 $\pm$ 1.1
		-30	27 $\pm$ 11	-40	25.7 $\pm$ 3.5		
H94 $\beta$ /H75 $\alpha$	26.6	+20	33.3 $\pm$ 7.7	+50	28.2 $\pm$ 4.2	+70	<b>23.9<math>\pm</math>0.6</b>
		-30	38 $\pm$ 14	-40	25.2 $\pm$ 4.6		

- <sup>(a)</sup> Estimated values assuming LTE conditions and optically thin radio continuum emission (see text).  
<sup>(b)</sup> The velocity components identified in  $LOS-0.11$  and  $LOS-0.02$  are labelled as +20 and -30 km s<sup>-1</sup>, and +50 and -40 km s<sup>-1</sup>, respectively. Only one velocity component labelled as +70 km s<sup>-1</sup> is identified in  $LOS+0.693$ .  
<sup>(c)</sup> Values or limits that do not match the expected LTE ratio are in bold print.

**Table 8.**  $Hem\beta/Hen\alpha$  ratios for  $LOS+0.693$ 

Ratio	Model <sup>(a)</sup> (%)	$\frac{I_{Hem\beta}}{I_{Hen\alpha}}$ (%)
He99 $\beta$ /He79 $\alpha$	27.3	25 $\pm$ 18
He98 $\beta$ /He78 $\alpha$	27.0	22.7 $\pm$ 7.8
He96 $\beta$ /He77 $\alpha$	27.7	22.1 $\pm$ 6.7
He96 $\beta$ /He76 $\alpha$	26.6	28.3 $\pm$ 7.0
He94 $\beta$ /He75 $\alpha$	26.6	<25.4

- <sup>(a)</sup> Estimated values assuming LTE conditions and optically thin radio continuum emission (see text).

## 4 DISCUSSION

### 4.1 Extended and diffuse RRL emission toward the three GC $LOS$

As previously mentioned, the only compact H II region which falls inside the GBT beam of our observations is toward  $LOS-0.02$ . This suggests that our GBT observations trace extended RRL emission toward  $LOS-0.11$  and  $LOS+0.693$ . In the case of  $LOS+0.693$ , this idea is also supported by the extended H69 $\alpha$  emission map of Sgr B2 shown in Fig. 6. This figure is obtained using the HOPS data (Purcell et al. 2012). The HOPS data has a spatial resolution of 2.4 arcmin at the frequency (19.59 GHz) of the H69 $\alpha$  line, which is a factor  $\sim 3$  worse than the average spatial resolution of our observations. Unfortunately, the HOPS data has a rms noise of  $\sim 40$  mK, which is not enough to obtain H69 $\alpha$  line emission maps for regions where both Sgr A sources were observed.

In order to figure out whether the emission detected by the GBT toward  $LOS-0.02$  is arising exclusively from the compact A region or not, we have compared the RRL emission measured using the VLA with that of our GBT observations. For this we have first determined the spectral index  $\alpha$  of the region A. This region shows a  $\alpha$  of  $0.06 \pm 0.04$  derived considering the  $S_c$  of  $590 \pm 30$  mJy that we have measured at 24.5 GHz (using the VLA map shown in Fig. 1) and

the value of  $570 \pm 20$  mJy derived at 14.7 GHz by Goss et al. (1985). Thus,  $T_A^* \propto \nu^{1.16}$  assuming that the free-free and RRL emission is optically thin. We have measured the H64 $\alpha$  peak line intensity of  $67 \pm 22$  mJy by integrating the channel map at the peak intensity of 47 km s<sup>-1</sup> (obtained using the data cube described in Section 2.1) over the HPBW of the GBT. By using the previous relation we have extrapolated the H64 $\alpha$  peak line intensity to that expected for the H76 $\alpha$  line, finding a  $T_A^*$  of  $39 \pm 12$  mJy at 14.7 GHz, which is similar to that of  $40.2 \pm 1.2$  mJy as measured by the GBT. This suggests that part of the region A inside the GBT beam may contribute significantly to the RRL emission detected in  $LOS-0.02$ . The  $T_A^*$  of  $39 \pm 12$  mJy found for the H76 $\alpha$  line is a factor  $\sim 2$  lower than that of 114 mJy as measured by Goss et al. (1985) for the entire region A, which agrees with the fact that only half of the region A falls inside the GBT beam size toward  $LOS-0.02$ . Despite this finding, we believe that it is unlikely that the GBT data traces extended RRL emission toward  $LOS+0.693$  and  $LOS-0.11$  and that it does not trace extended RRL emission toward  $LOS-0.02$ . In fact this is supported in Fig. 7 (upper panel) where we show the C I, C II and H79 $\alpha$  spectra of  $LOS-0.11$  and  $LOS-0.02$ . It can be seen that both the positive and negative velocity components of the extended ionised gas traced by the C II emission (García 2015) are also well traced by the H79 $\alpha$  line emission. Therefore, in this paper we consider that the GBT traces extended ionised gas in the three  $LOS$ s.

The studied ionised gas is also diffuse because we have found  $n_e$  of  $\sim 40-310$  cm<sup>-3</sup>, which are much lower than those of  $3600-5100$  cm<sup>-3</sup> found in compact H II regions of the GC (Mills et al. 2011). The  $n_e$  of  $\sim 40-120$  cm<sup>-3</sup> found for the negative velocity gas of  $LOS-0.11$  and  $LOS-0.02$  are consistent with those of  $\sim 100-130$  cm<sup>-3</sup> found for diffuse ionised gas of the Arched Filaments H II complex (Langer et al. 2017).

C II emission traces a negative velocity component not only in both Sgr A sources but also in the H I source and Sgr A\* (see the bottom panel of Fig. 7). We also note in Fig. 7 that the C I emission does not trace the negative ve-

**Table 9.** Helium-to-hydrogen line intensity ratios for the three GC sources

Ratio	$LOS-0.11$		$LOS-0.02$		$LOS+0.693$	
	$v_r^{(a)}$ (km s <sup>-1</sup> )	$\frac{I_{He n\alpha}}{I_{H n\alpha}}$ (%)	$v_r^{(a)}$ (km s <sup>-1</sup> )	$\frac{I_{He n\alpha}}{I_{H n\alpha}}$ (%)	$v_r^{(a)}$ (km s <sup>-1</sup> )	$\frac{I_{He n\alpha}}{I_{H n\alpha}}$ (%)
He79 $\alpha$ /H79 $\alpha$	+20	<20	+50	<10	+70	7.2 $\pm$ 0.5
	-30	<40	-40	<20		
He78 $\alpha$ /H78 $\alpha$	+20	<10	+50	<10	+70	9.0 $\pm$ 0.7
	-30	<20	-40	<20		
He77 $\alpha$ /H77 $\alpha$	+20	<50	+50	<10	+70	7.4 $\pm$ 1.0
	-30	<100	-40	<20		
He76 $\alpha$ /H76 $\alpha$	+20	<20	+50	<10	+70	6.1 $\pm$ 0.5
	-30	<30	-40	<20		
He75 $\alpha$ /H75 $\alpha$	+20	<20	+50	<10	+70	6.9 $\pm$ 1.5
	-30	<30	-40	<20		
He99 $\beta$ /H99 $\beta$	+20	<50	+50	<40	+70	7.6 $\pm$ 3.8
	-30	<70	-40	<90		
He98 $\beta$ /H98 $\beta$	+20	<30	+50	<10	+70	10.5 $\pm$ 2.3
	-30	<80	-40	<30		
He97 $\beta$ /H97 $\beta$	+20	<40	+50	<10	+70	9.0 $\pm$ 3.1
	-30	<100	-40	<30		
He96 $\beta$ /H96 $\beta$	+20	<40	+50	<10	+70	9.1 $\pm$ 1.4
	-30	<80	-40	<30		
He95 $\beta$ /H95 $\beta^{(b)}$	+20	...	+50	...	+70	8.5 $\pm$ 1.4
	-30	...	-40	...		
He94 $\beta$ /H94 $\beta$	+20	<60	+50	<30	+70	<8.3
	-30	<90	-40	<50		

<sup>(a)</sup>The velocity components identified in  $LOS-0.11$  and  $LOS-0.02$  are labelled as +20 and -30 km s<sup>-1</sup>, and +50 and -40 km s<sup>-1</sup>, respectively. Only one velocity component labelled as +70 km s<sup>-1</sup> is identified in  $LOS+0.693$ .

<sup>(b)</sup>The He95 $\beta$ /H95 $\beta$  line intensity ratios for both sources of Sgr A were not measured because the He95 $\beta$  RRL was not observed.

**Table 10.** Physical properties derived for the three GC sources

Source	RRL	$v_r^{(a)}$ (km s <sup>-1</sup> )	$S_c$ (mJy)	$n_e$ (cm <sup>-3</sup> )	$\log(N_{Ly\alpha})$ (ph. s <sup>-1</sup> )
$LOS-0.11$	H77 $\alpha$	+20	122 $\pm$ 23	71 $\pm$ 7	47.14 $\pm$ 0.08
		-30	153 $\pm$ 40	80 $\pm$ 10	47.24 $\pm$ 0.10
	H96 $\beta$	+20	42 $\pm$ 14	43 $\pm$ 7	46.70 $\pm$ 0.12
		-30	35 $\pm$ 13	39 $\pm$ 7	46.62 $\pm$ 0.14
$LOS-0.02$	H77 $\alpha$	+50	451 $\pm$ 18	137 $\pm$ 3	47.71 $\pm$ 0.02
		-40	339 $\pm$ 25	119 $\pm$ 4	47.58 $\pm$ 0.03
	H96 $\beta$	+50	118 $\pm$ 9	72 $\pm$ 3	47.15 $\pm$ 0.03
		-40	96 $\pm$ 11	65 $\pm$ 4	47.06 $\pm$ 0.05
$LOS+0.693$	H77 $\alpha$	+70	2311 $\pm$ 45	310 $\pm$ 3	48.42 $\pm$ 0.01
	H96 $\beta$	+70	603 $\pm$ 19	163 $\pm$ 3	47.86 $\pm$ 0.01

<sup>(a)</sup>The velocity components identified in  $LOS-0.11$  and  $LOS-0.02$  are labelled as +20 and -30 km s<sup>-1</sup>, and +50 and -40 km s<sup>-1</sup>, respectively. Only one velocity component labelled as +70 km s<sup>-1</sup> is identified in  $LOS+0.693$ .

locity component in  $LOS-0.11$  and  $LOS-0.02$  but it does partially in the H1 source and Sgr A\*.

## 4.2 Kinematics of the ionised gas

Our RRLs show diffuse ionised gas with negative and positive velocities in  $LOS-0.11$  and  $LOS-0.02$ . In Fig. 8 we show the velocities of both Sgr A sources on a position-velocity diagram for the C II emission. Four gas streams from the model of Kruijssen et al. (2015) are also shown in this figure. The  $v_r$  of both velocity components of  $LOS-0.11$  are consistent with the velocities of streams 1 and 4, while the  $v_r$  of both velocity components of  $LOS-0.02$  agree with the velocities of streams 1 and 2. This suggests that along the

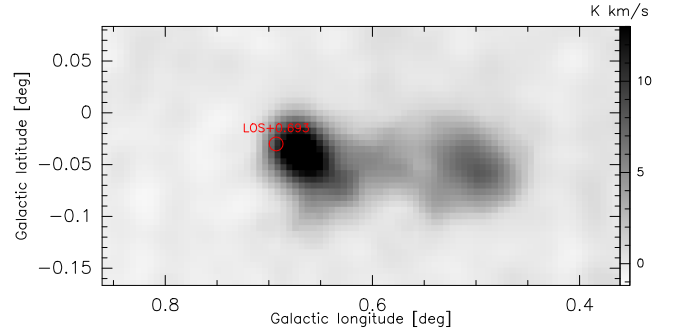


**Figure 6.** H69 $\alpha$  integrated line emission of Sgr B2 obtained using HOPS data (Purcell et al. 2012). The range of velocity integration is from 20 to 80 km s<sup>-1</sup>.  $LOS+0.693$  is indicated with a red circle with the size of the HPBW of the GBT observations (48 arcsec at 13.09 GHz).

two  $LOS$ s the GBT traces diffuse and extended ionised gas that are part of the gas streams orbiting the GC. The positions of  $LOS-0.11$  and  $LOS-0.02$  (see Fig. 8, upper panel) also support that the positive velocity gas in both sources is part of stream 1. The velocities and positions of the regions H1–H5 (see Fig. 8) show that these sources are likely associated with stream 2. If this hypothesis is correct then the negative velocity gas of  $LOS-0.02$  could coexist with the H1–H5 sources. Our hypothesis is in agreement with the finding of Langer et al. (2017) that the kinematics of the



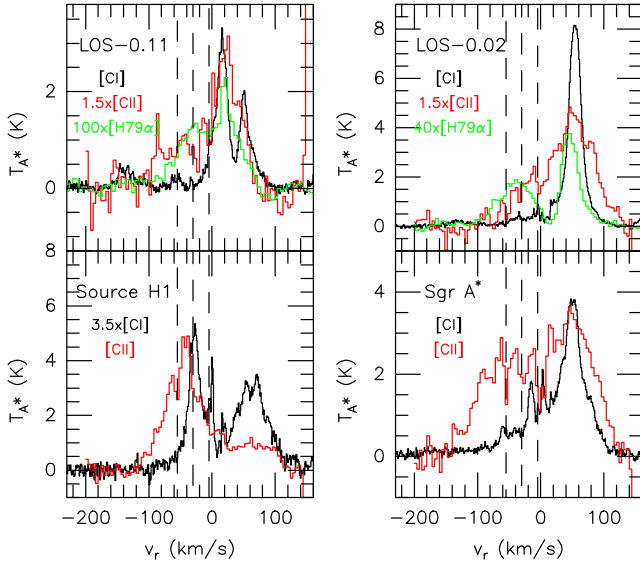


**Figure 7.** Upper panels: CI (black), CII (red) and H79 $\alpha$  (green) spectra observed toward  $LOS-0.11$  and  $LOS-0.02$ . Bottom panels: CI (black) and CII (red) spectra observed toward the H1 source and Sgr A\*. The line intensity of several spectra is multiplied by a factor for comparison purposes. CII spectra is affected by absorption features (indicated by dashed lines) associated with the 3 kpc, 4.5 kpc and local spiral arms (Oka et al. 1998). The CI and CII spectra are obtained with a spatial resolution of 46 arcsec similar to that of the H79 $\alpha$  spectra.

ionised gas in the Sgr A and Sgr B2 complexes, as traced by the CII emission, is well explained by the gas streams proposed by Kruijssen et al. (2015).

### 4.3 Sources of ionisation

#### 4.3.1 Positive velocity gas in the three GC LOSs

The ionised gas studied in  $LOS-0.11$  is at a projected distance of  $\sim 3.8$  pc from the region G (see Fig. 1), whose massive stars are thought to be the closest compact source of ionisation to the positive velocity  $LOS-0.11$  gas (Ho et al. 1985). On the other hand, since the region L lies close to  $LOS+0.693$  (see Fig. 1, bottom panel), it is expected that the main ionisation source of the  $LOS+0.693$  gas could be the massive stars responsible for the ionisation of the region L.

As can be seen in the upper panel of Fig. 1, part of the emission arising in the region A falls within the GBT beam toward  $LOS-0.02$ . Thus we expect that the gas with positive velocities in this GC source is mainly ionised by the massive stars in the HII region A. To test whether the HII region A could be the main source of ionisation of the positive velocity gas in  $LOS-0.02$  we estimate the number of photons inside the GBT beam,  $N_\Omega$ , and that  $\sim 50\%$  of the region A falls inside the GBT beam (see Fig. 1). Considering the location of the GBT beam centre, then the compact HII region A would actually be displaced from the telescope beam centre. For this geometry we can esti-

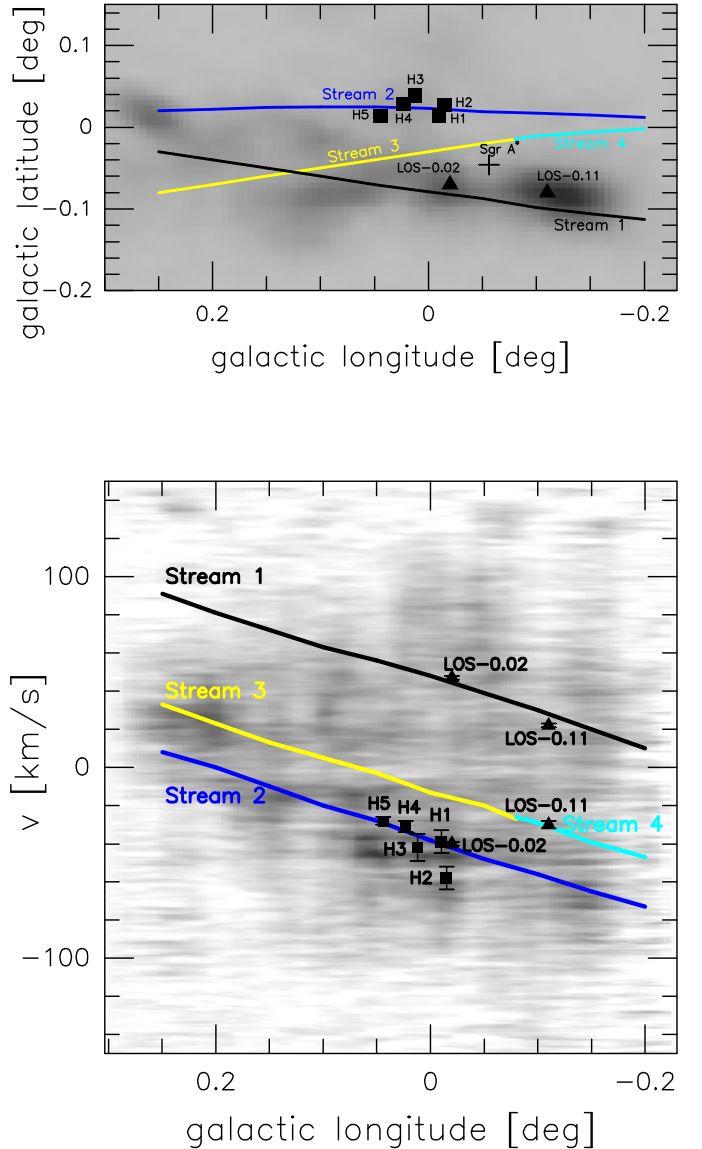


**Figure 8.** Upper panel: Four streams used to model the GC gas kinematics (Kruijssen et al. 2015). The  $NH_3(1,1)$  emission map obtained using HOPS data (Purcell et al. 2012) is shown in gray scale. The map is integrated over the velocity range  $-100$  to  $+100$  km s $^{-1}$ . Filled triangles indicate positions of  $LOS-0.11$  and  $LOS-0.02$ , while filled squares show the positions of H1–H5 sources. The black cross shows the position of Sgr A\*. Bottom panel: The four streams are drawn on the position-velocity CII map obtained using HIFI data (García et al. 2016). This map covers  $0.1^\circ$  in latitude centered at  $0^\circ$ . Central line velocities of  $LOS-0.11$  and  $LOS-0.02$  are shown with filled triangles, while the central line velocities of H1–H5 sources (Zhao et al. 1993) are indicated with filled squares. Velocity error bars overlap with filled triangles.

mate an upper limit to  $N_\Omega$  following the expression given by Rodríguez-Fernández & Martín-Pintado (2005):

$$N_\Omega = \frac{N_{Lyc}}{4\pi r^2} \Omega D^2, \quad (3)$$

where  $r$  is the radius of the HII region. We derive the upper

limit of  $10^{50.95}$  photons  $\text{s}^{-1}$  for the value of  $N_{\Omega}$  by using the  $N_{\text{Lyc}}$  value provided by Mills et al. (2011) for the HII region A,  $\Omega=45$  arcsec and  $r=1.7$  pc in Eq. 3. It seems that the positive velocity gas of  $LOS-0.02$  is mainly ionised by the massive stars in the HII region A because the  $N_{\text{Lyc}}$  values of  $LOS-0.02$ , given in Table 10, are consistent with the upper limit of  $10^{50.95}$  photons  $\text{s}^{-1}$ .

#### 4.3.2 Negative velocity gas in $LOS-0.11$ and $LOS-0.02$

The ionised gas components with negative velocities found toward both sources of Sgr A raises the question of the source of ionisation. The top-down view shown in Fig. 6 of Kruijssen et al. (2015) gives us information about the distances between Sgr A\* and the four streams considered in their kinematical model. In this scenario Sgr A\* is located between both the 20 and 50  $\text{km s}^{-1}$  clouds and their background gas streams 3 and 4, at a projected distance of  $\sim 60$  pc from these features. If the negative velocity  $LOS-0.02$  gas is part of the gas stream 2, as discussed in Section 4.2, then it may be ionised by the photons arising in massive O6–O7 stars which also ionise the presumably closest UC–HII regions, i.e. H1–H5 (Zhao et al. 1993), located at least  $\sim 12$  pc away from the negative velocity gas observed toward  $LOS-0.02$  (see Fig. 8, upper panel). Of course, other ionising sources apart from those proposed may exist in the environment of the negative velocity  $LOS-0.11$  gas. On the other hand, the negative velocity  $LOS-0.02$  gas is likely part of the stream 4, as discussed in Section 4.2. So far there are no compact HII regions or massive stars whose velocities and positions are consistent with those of the gas stream 4 around  $LOS-0.11$ , hence the identification of ionising sources of the negative velocity  $LOS-0.11$  gas remains unclear. A possibility is that the negative velocity  $LOS-0.11$  gas is actually part of stream 2, despite the difference in their velocities (see Fig. 8, bottom panel), thus being also ionised by the massive stars inside H1–H5 sources as for  $LOS-0.02$ .

Considering the gas stream model proposed by Kruijssen et al. (2015) the massive young stars orbiting Sgr A\* can be ruled out as ionising sources of the negative velocity  $LOS-0.11$  and  $LOS-0.02$  gas since in this scenario Sgr A\* is  $\sim 60$  pc away from gas streams 2 and 4 along the two  $LOS$ s.

## 5 CONCLUSIONS

Using the GBT telescope we have detected extended and diffuse ionised emission toward three GC  $LOS$ s. The main conclusions of the present work are as follows:

- We found that the ionised gas observed toward the three GC sources is emitted under LTE conditions based on the  $Hm\beta$ –to– $Hn\alpha$  integrated line intensity ratios.
- We found a  $^4\text{He}$  mass fraction  $Y$  of  $0.29 \pm 0.01$  that supports the hypothesis that high-mass stars in the GC have enriched the helium–4 abundance in the ISM as compared to the primordial value.
- For  $LOS-0.11$ ,  $LOS-0.02$  and  $LOS+0.693$  we have derived  $n_e$  and  $N_{\text{Lyc}}$  values. The studied gas is characterised by  $n_e$  of  $\sim 40$ – $310 \text{ cm}^{-3}$ .

- The ionised gas detected toward regions of the 20 and 50  $\text{km s}^{-1}$  clouds is likely associated, following the Kruijssen et al. (2015) model, with gas stream 1 orbiting the GC, while the ionised gas moving with negative velocities in  $LOS-0.02$  and  $LOS-0.11$  is likely associated with the gas streams 2 and 4, respectively, located in projection  $\sim 12$  pc above stream 1.

- The  $LOS-0.02$  gas at positive velocities is mainly ionised by UV photons produced in the massive stars also ionising the HII region A. The massive stars inside the HII regions L and G are considered the closest sources of gas ionisation of  $LOS+0.693$  and  $LOS-0.11$  (positive velocity component), respectively.

- We propose that the gas with negative velocities observed toward  $LOS-0.02$  may be ionised by UV photons originating in the massive stars of the presumably closest HII regions H1–H5.

- The negative velocity gas observed toward  $LOS-0.11$  is likely associated with gas stream 4. We were not able to propose any possible ionising sources of the negative velocity  $LOS-0.11$  gas because, so far, there are no compact HII regions or massive stars having both velocities and positions similar to those expected for gas stream 4 around  $LOS-0.11$ . However, if the negative velocity components of both Sgr A sources are part of the stream 2, then the massive stars in the H1–H5 regions could be the main sources of UV photons ionising the gas with negative velocities of both Sgr A sources.

- We compared CI spectra with our H79 $\alpha$  spectra, finding that CI emission does not trace the negative velocity component of either of the Sgr A sources. This indicates that this diffuse gas component is fully ionised.

## ACKNOWLEDGEMENTS

We thank the anonymous referee for comments which helped to improve this paper. A. Báez-Rubio acknowledges support from a DGAPA postdoctoral grant (year 2015) to UNAM. J.M.-P. acknowledges partial support by the MINECO under grants ESP2015–65597–C4–1 and ESP2017– and Comunidad de Madrid grant number S2013/ICE–2822 SpaceTec–CM.

## REFERENCES

- Armstrong D. A., Jackson J. M., Ho P. T. P., 1989, IAU Symp. 136, The Center of the Galaxy, ed. M. Morris (Dordrecht: Kluwer), 389
- Bally J., Stark A. A., Wilson R. W., 1987, ApJS, 65, 13
- Báez-Rubio A., Martín-Pintado J., Thum C., Planesas P., 2013, A&A, 553, A45
- Boehel A., Ghez A. M., Schödel R., Meyer L., Yelda S., Albers S., Martinez S., Becklin G. D., Do. T., Lu J. R., Matthews K., Morris M. R., Sitarski B., Witzel G., 2016, ApJ, 830, 17
- Coc A., Gorieli S., Xu Y., Saimpert M., Vangioni E., 2012, ApJ, 744, 158
- De Pree C. G., Wilder D. J., Deblasio J., Mercer A. J., Davis L. E., 2005, ApJ, 624, L101
- Ekers R. D., van Gorkom J. H., Schwarz U. J., Goss W. M., 1983, A&A, 122, 143
- García P., 2015, PhD thesis, University of Cologne, Germany: <http://kups.ub.uni-koeln.de/6358/>

- García P., Simon R., Stutzki J., Güsten R., Requena-Torres M. A., Higgins R., 2016, *A&A*, 588, A131
- Gaume R. A., Claussen M. J., De Pree C. G., Goss W. M., Mehringer D. M., 1995, *ApJ*, 449, 663
- Gordon M. A., Berkemann U., Mezger P. G., Zylka R., Haslam C. G. T., Kreysa E., Sievers A., Lemke R., 1993, *A&A*, 280, 208
- Gordon M. A., Sorochenko R. L., 2009, *Radio Recombination Lines: Their Physics and Astronomical Applications* (New York: Springer)
- Goss W. M., Schwarz U. J., van Gorkom J. H., Ekers R. D., 1985, *MNRAS*, 215, 69
- Henshaw J. D., et al., 2016, *MNRAS*, 457, 2675
- Ho P. T. P., Jackson J. M., Barrett A. H., Armstrong J. T., 1985, *ApJ*, 288, 17
- Kruijssen J. M. D., Dale J. E., Longmore S. N., 2015, *MNRAS*, 447, 1059
- Lang C. C., Goss W. M., Morris M., 2001, *AJ*, 121, 2681
- Langer W. D., Velusamy T., Morris M. R., Goldsmith P. F., Pineda J. L., 2017, *A&A*, 599, A136
- Lau R. M., Herter T. L., Morris M. R., Adams J. D., 2014, *ApJ*, 794, 108
- Martín S., Requena-Torres M. A., Martín-Pintado J., Mauersberger R., 2008, *ApJ*, 678, 245
- Lu F. J., Wang Q. D., Lang C. C., 2003, *AJ*, 126, 319
- Molinari A. et al., 2011, *ApJL*, 735, L33
- Mills E., Morris M. R., Lang C. C., Dong H., Wang Q. D., Cotera A., Stolovy S. R., 2011, *ApJ*, 735, 84
- Mehringer D. M., Palmer P., Goss W. M., Yusef-Zadeh F., 1993, *ApJ*, 412, 684
- Mezger P. G., Henderson A. P., 1967, *ApJ*, 147, 471
- Purcell C. R. et al. 2012, *MNRAS*, 426, 3
- Oka T., Hasegawa T., Sato F., Tsuboi M., Miyazaki A., 1998, *ApJS*, 118, 455
- Rodríguez-Fernández N. J., Martín-Pintado J., 2005, *A&A*, 429, 923
- Royster M. J., Yusef-Zadeh F. 2014, in Sjouwerman L., Ott J., Lang C., eds, *Proc. IAU Symp. 303, The Galactic Center: Feeding and Feedback in a Normal Galactic Nucleus*. p. 92
- Roelfsema P. R., Goss W. M., Whiteoak J. B., Gardner F. F., Pankonin V., 1987, *A&A*, 175, 219
- Rohlfs K., Wilson T. L., 1999, *Tools of Radio Astronomy* (Heidelberg: Springer-Verlag)
- Spitzer L., 2004, *Physical processes in the Intertellar Medium*, Wiley-VCH, p. 107
- Serabyn E., Lacy J. H., Achtermann J. M., 1992, *ApJ*, 395, 166
- Tsvilev A. P., Parfenov S. Yu., Sobolev A. M., Krasnov V. V., 2013, *Astron. Lett.*, Springer, 39, 737
- Towle J. P., Feldman P. A., and Watson J. K. G., 1996, *ApJS*, 107, 747
- Wilson T. L., Rood R. T., 1994, *ARA&A*, 32, 191
- Yusef-Zadeh F., Wardle M., Muno M., Law C., Pound M., 2005, *Advances in Space Research*, 35, 1074
- Zhao J.-H., Desai K., Goss W. M., Yusef-Zadeh F., 1993, *ApJ*, 418, 235

This paper has been typeset from a  $\text{\LaTeX}$  file prepared by the author.